

Article

# Advanced Fabrication of Single-Mode and Multi-Wavelength MIR-QCLs

Martin J. Süess<sup>1</sup>, Romain Peretti<sup>1</sup>, Yong Liang<sup>1</sup>, Johanna M. Wolf<sup>1</sup>, Christopher Bonzon<sup>1</sup>, Borislav Hinkov<sup>1</sup>, Selamnesh Nida<sup>1</sup>, Pierre Jouy<sup>1</sup>, Wondwosen Metaferia<sup>2</sup>, Sebastian Lourduoss<sup>3</sup>, Mattias Beck<sup>1</sup> and Jérôme Faist<sup>1,\*</sup>

<sup>1</sup> Institute for Quantum Electronics, ETH Zürich, Ch-8093 Zurich, Switzerland; martin.suess@phys.ethz.ch (M.J.S.); perettir@phys.ethz.ch (R.P.); liangyo@phys.ethz.ch (Y.L.); wolfjo@phys.ethz.ch (J.M.W.); bonzonc@phys.ethz.ch (C.B.); borislav.hinkov@tuwien.ac.at (B.H.); nida@aps.ee.ethz.ch (S.N.); pjouy@phys.ethz.ch (P.J.); mattias.beck@phys.ethz.ch (M.B.)

<sup>2</sup> Solid State Physics, Lund University, Box 118, SE'221 00 Lund, Sweden; wondwosen.metaferia@ftf.lth.se

<sup>3</sup> Laboratory of Semiconductor Materials, School of ICT, KTH-Royal Institute of Technology, 164 40 Kista, Sweden; slo@kth.se

\* Correspondence: jerome.faist@phys.ethz.ch; Tel.: +41-044-633-7280

Received: 22 March 2016; Accepted: 2 May 2016; Published: 11 May 2016

**Abstract:** In this article we present our latest work on the optimization of mid-infrared quantum cascade laser fabrication techniques. Our efforts are focused on low dissipation devices, broad-area high-power photonic crystal lasers, as well as multi-wavelength devices realized either as arrays or multi-section distributed feedback (DFB) devices. We summarize our latest achievements and update them with our most recent results.

**Keywords:** quantum cascade lasers; mid-infrared; semiconductor fabrication; mode control; high performance; multi-wavelength; laser arrays

## 1. Introduction

Since the first demonstration [1] of the quantum cascade laser (QCL) over two decades ago, the surrounding technology has vastly improved, as proven by room temperature continuous wave (CW) operation [2], high optical power [3], low dissipation devices [4–6], and extended accessible spectral range [7–11]. These achievements can unambiguously be attributed to the extensive work on fabrication and design strategies with the aim to optimize thermal transport in the structures, to reduce the electrical footprint of the active waveguide, to decrease electrical and scattering losses due to an improved material quality, while simultaneously amplifying the power [12–17], as well as to continued optimization of the quantum cascade structure serving as the gain medium in QCLs [18–22].

In this mature field, the present-day direction of research is to address the requirements of potential applications, such as trace gas spectroscopy [23–25], defense countermeasures [26–28], micro-surgery [29,30], and optical free-space communication [31–33]. These technologically-challenging implementations typically call for a precise and stable mode control, high efficiency, and good beam shape. In this short review, we summarize the recent achievements in the areas of QCL fabrication at ETH Zurich and update recent results with the latest experimental data.

The paper is organized as follows: in Section 2 we summarize our work on active region growth and highlight the tools we use for their characterization. In Section 3 we discuss our efforts to optimize the waveguide fabrication. Section 4 treats the different epitaxial regrowth steps in the fabrication process, and the doping engineering performed to optimize them. In Section 5 we implement all optimizations and show our results on low dissipation short-wavelength QCLs with excellent mode control. In Section 6 we apply a mode control strategy to fabricate multi-wavelength QCL arrays

and demonstrate how a monolithically bonded collector chip can combine the different wavelengths in a single beam of light. In Section 7 we then present an alternative device concept that allows the emission of few wavelengths together or independently without the need to bond an additional chip for the light collection. Section 8 then describes our efforts on fabricating buried photonic crystal QCLs. We then conclude our results in Section 9.

## 2. Active Region Growth and Material Characterization

First and foremost, the performance of QCLs is strongly dependent on the active layer, from which the light is emitted. One of the main aspects in realizing efficient QCL active regions is a rigorous control of the molecular beam epitaxy (MBE) growth process. A good control of the active region growth can be achieved by an adequate mixture of characterization techniques covering both global and local resolution. Here, the term “global” refers to length scales ranging from 100  $\mu\text{m}$  to 1 cm, a high degree of information averaging over more than one dimension, resulting in a good sensitivity. The term “local” refers to length scales ranging from 1  $\text{\AA}$  to 10  $\mu\text{m}$  and information averaging over one dimension, at most, resulting in a limited sensitivity. The typical instrumentation used for this purpose is listed in Table 1 and is qualitatively assessed with respect to its capability to deliver a specific type of information on the respective length scale.

**Table 1.** Summary of methods used for material characterization of the active region.

Method	Information	Global <sup>1</sup>	Local <sup>1</sup>
Laboratory X-ray Diffraction (XRD)	Crystallinity, strain, periodicity, average alloy concentration	++	–
Transmission Electron Microscopy (TEM)	Nanostructure morphology, layer thickness, crystallinity, interface quality	–	++
Atom Probe Tomography (APT)	Nanostructure morphology, 3D alloy concentration	–	++
Scanning Electron Microscopy (SEM)	Microstructure morphology, size, roughness	+	+
Secondary Ion Mass Spectroscopy (SIMS)	1D alloy composition	++	–

<sup>1</sup> ++: highly capable, +: capable with limitations, –: incapable.

Figure 1 contains a collection of data recorded with laboratory X-ray diffraction (XRD), transmission electron microscopy (TEM), and atom probe tomography (APT) for an active region operating around 3.1–3.3  $\mu\text{m}$ . The XRD measurements (Figure 1a) disclose global information, such as the average periodicity of the active region over the whole wafer, average alloy concentrations, as well as deviations from center to border of the wafer and the beginning to end of the growth; e.g., from the position of the 0th order superlattice peak relative to the substrate peak, it can be determined, whether strain relaxation has occurred during the growth. Additionally, from the spacing of the superlattice peaks, the total period thickness can be determined and compared to the designed period thickness. Complementarily, TEM measurements can resolve the superlattice with high local magnification, even down to the atomic scale (Figure 1b), and reveal the local morphology (e.g., interface roughness) of the layers (Figure 1c).

Chemical information can be obtained by APT measurements, which can deliver the three-dimensional distribution of chemical species (Figure 1d). This is of particular interest when segregation or depletion of particular elements is studied, and the location and size of the resulting clusters are of interest. On the other hand, if the epitaxial growth is of very high quality, this representation of data can be used e.g., for determination of the chemical roughness of interfaces. Quantitative information about the local concentration of the different elements in growth direction

can be found in averaged chemical profiles (Figure 1e) extracted from the three-dimensional datasets (Figure 1d). Such profiles are similar to secondary ion mass spectroscopy data but are limited in sensitivity to ppm levels. In general, the data retrieved from these measurements deliver valuable information for the adjustment of the fractional concentration of indium, gallium and aluminum, which is crucial for structural properties, such as strain balancing and interface quality, as well as electronic properties, such as band offsets and discontinuities.

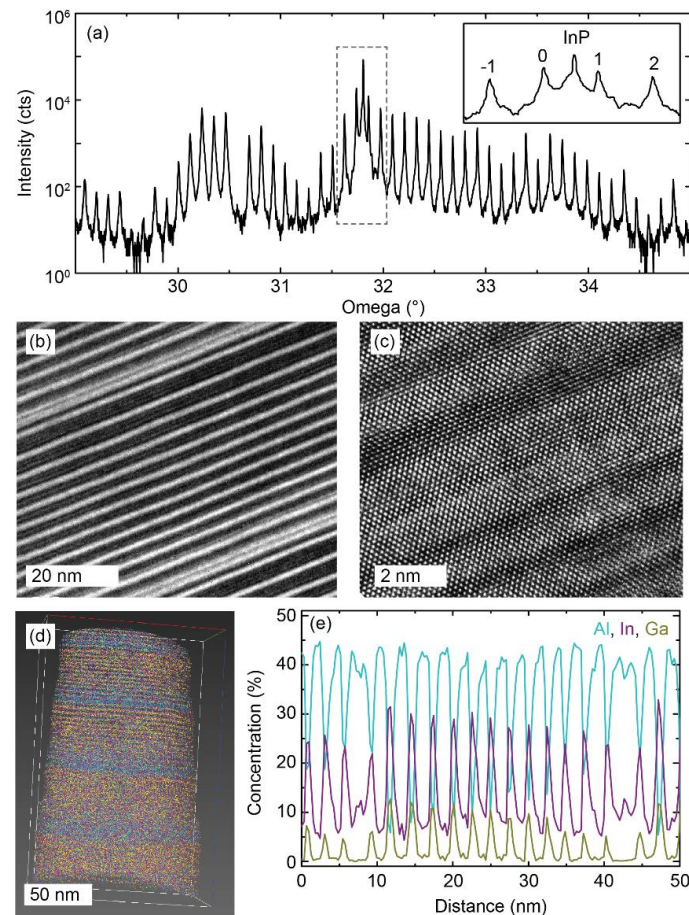


**Figure 1.** Summary of material characterization techniques for QCLs. (a) XRD symmetric scan giving information about the out-of-plane lattice constants, the average periodicity of the superlattice and strain relaxation. The inset displays a zoom of the data inside the gray dashed box, where the substrate peak (InP) and the  $-1$ st to 2nd order superlattice peaks are indicated; (b) dark-field TEM image resolving the QCL superlattice locally, where the thinnest resolved barrier layer amounts to  $5 \text{ \AA}$ ; (c) high-resolution TEM showing the interfaces between individual layers of the superlattice; (d) three-dimensional reconstruction of an APT measurement resolving four superlattice periods; and (e) averaged one-dimensional concentration profile extracted from the APT data displayed in (d).

### 3. Waveguide Fabrication

In addition to the active region design, the QCL performance depends on the implementation into a waveguide structure, which is responsible for efficient current driving in the structure and the build-up of the optical modes. Since QCLs are specifically interesting for spectroscopic applications, the desirable performance attributes are precise mode control, low power dissipation, and high slope efficiency, as well as continuous wave operation. In order to achieve these characteristics, the processing of the waveguide has to be developed carefully. In this section we will use the term “standard” to denote typical inverted buried heterostructure (IBH) process steps [34], and the term “optimized” to denote process steps that have been modified to address the aforementioned requirements.

Starting from an active region layer, the first step in an iBH process [34] for single-mode devices is the photolithographic definition and wet-chemical etching of the DFB grating (Figure 2a). For short wavelength emission (e.g., 3.3  $\mu\text{m}$ ) the size of the smallest grating features (260 nm) is close to the illumination wavelength (220 nm) of the mask aligner, as shown in the scanning electron microscope (SEM) image in Figure 2b. Optical lithography steps with such narrow features are susceptible to inhomogeneous contact between the mask and sample. The resulting Newton's rings (cf. Figure 2a) disrupt the grating pattern and result in modified emission wavelengths or parasitic modes in the final device. In order to minimize such effects in this lithography step, we use a diluted resist (AZ1505:EBR = 1:4), resulting in a resist thickness of 70 nm. The resist layer was exposed with a dose of 7 mJ/cm<sup>2</sup> on a Deep-UV mask aligner (ABM Inc., Scotts Valley, CA, USA) operating at 220 nm. The exposed resist was developed with a diluted KOH solution (1 M KOH:H<sub>2</sub>O = 1:8) for 35 s.

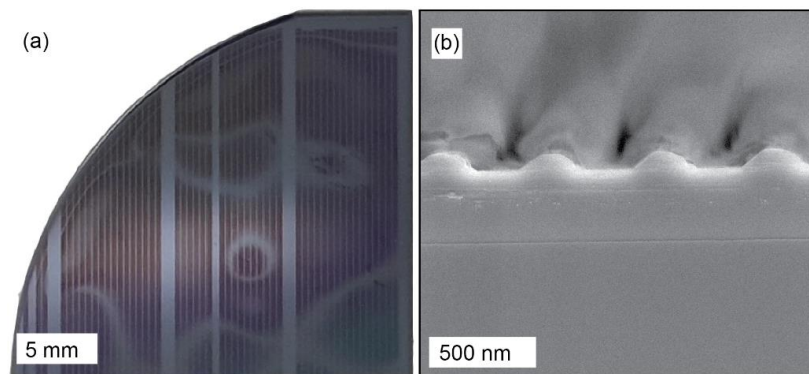


**Figure 2.** Grating lithography (a) a quarter two-inch InP-based QCL wafer with a lithography resist for a grating. The resist pattern is disrupted by Newton's rings; and (b) cross-sectional SEM micro graph of the grating lithography after wet etching with a low-end feature size of ~260 nm.

In the next process step, the active core is obtained via an oxide hard mask and a wet etching step. The etching of the active waveguide requires an etchant which isotropically etches InP and the QC active region composed of ternary InGaAs and AlInAs alloys. This requirement is also necessary to provide a smooth active waveguide profile for the lateral MOVPE regrowth (discussed in the next section). In the standard iBH process HBr:HNO<sub>3</sub>:H<sub>2</sub>O (1:1:10) is used for this etch step. This etchant requires an "aging" period of 10–14 days and is sensitive to visible and ultraviolet light, which can easily result in an unbalanced material selectivity. Such an imbalance can result in etch profiles at the edge of the active region featuring an unwanted sidewall roughness, as can be seen in Figure 3a,b. The structures displayed in Figure 3a,b were covered with an oxide to enhance the contrast for the TEM micrographs and to highlight the roughness created through this etch step. When such structures are overgrown with MOVPE, the roughness can in turn lead to the occurrence of stacking faults during regrowth (indicated with red arrows in Figure 3c,d), which can deteriorate the electrical properties of the regrowth, by creating electrical leakage paths.

To optimize this etch step we use a diffusion-limited etching mixture of HBr:Br:H<sub>2</sub>O (17:1:10), which provides a uniform, fast, and deep etching with smooth side walls, and creates a sufficiently large overhang of the oxide mask required for the selective MOVPE regrowth. Additionally, the width of the active waveguide can be controlled within a maximum deviation of 20% (Figure 3e), which enables the fabrication of narrow waveguides required for low dissipation devices and a better prediction of the effective refractive index of the lasing mode, which is beneficial for precise mode control. Furthermore, sufficiently long etching can yield a rectangular shape of the active region (as opposed to a trapezoidal shape). In Figure 3f, we show an active region of 30 active periods (layer contrast) sandwiched between two InGaAs claddings, after optimized etching, including lateral and cladding MOVPE regrowth. Since, in such rectangular shaped active cores, each period of the

quantum cascade has a similar width, the current distribution is more uniform, which results in a similar alignment voltage for each period. Consequently, the overall device performance improves.

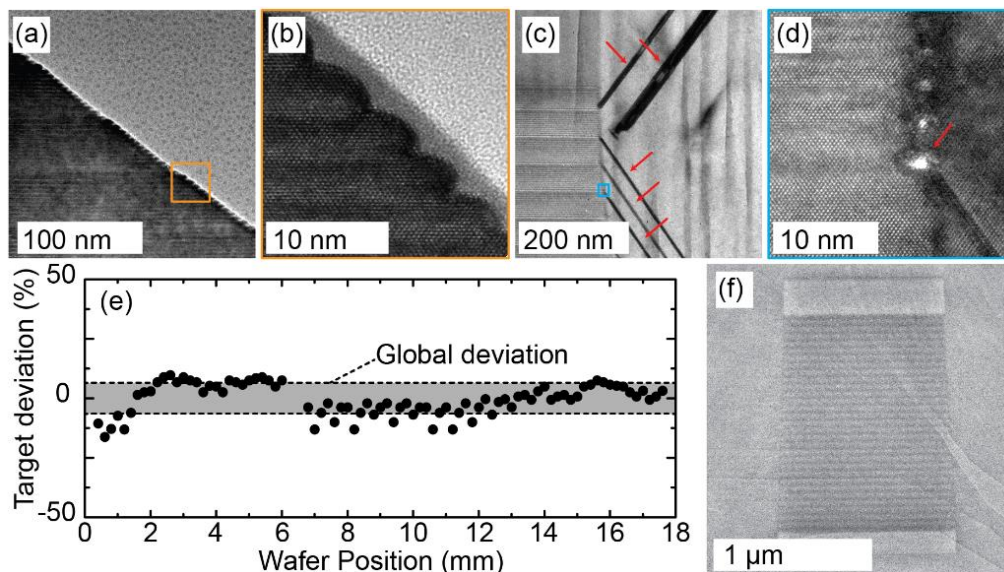


**Figure 3.** Analysis of waveguide definition. (a) TEM micrograph depicting the sidewall of an etched active region; and (b) high-resolution TEM showing a detail marked with an orange box in (a). (c) Dark-field TEM image depicting stacking faults (red arrows) originating at the interface between the active region and the lateral MOVPE regrowth; (d) high-resolution TEM showing a zoom to a stacking fault marked with a blue box in (c). The red arrow highlights the stacking fault nucleation site; (e) deviation from the target active waveguide width as a function of position on the wafer; and (f) cross-sectional SEM micrograph of a  $\sim 1 \mu\text{m}$  wide buried active waveguide; (a–d) are data retrieved from standard process samples; (e,f) from optimized process samples.

#### 4. Epitaxial Regrowth

Typically, an iBH process foresees two metal-organic vapor phase epitaxy (MOVPE) regrowth steps: one regrowth to laterally insulate the active region from leakage currents (“lateral”), and a second regrowth acting as an optical cladding with minimized free carrier absorption, while reducing electrical barriers for proper injection of electrons into the active region (“cladding”). However, the material thickness of the lateral regrowth is limited by the orientation-dependent growth rate and the transport of gaseous precursor species to the side of the active core. The overhanging oxide hard-mask needed for the selective growth, and the etch profile of the active core can result in a reduced material thickness close to the upper edges of the active region. In this case the material thickness is thin enough to allow carrier tunneling through the interface between the active region and the lateral regrowth resulting in an insufficient electrical insulation. In order to reduce these leakage paths, the thickness of the insulating regrowth is increased by adding a further regrowth after the wet etching of the grating and before the definition of the active core (“planarization”), and is effectively turning the iBH process into a buried iBH process (BiBH). The planarization regrowth shares the requirements of the cladding and therefore needs to be electrically conducting while having a low enough doping to reduce free carrier absorption. SEM micrographs of the facets of a device with and a device without the planarization regrowth are compared in Figure 4a. The two images are schematically redrawn in Figure 4b, in order to indicate the increased material thickness of the lateral regrowth close to the active region due to the planarization regrowth. The red arrows schematically indicate the potential magnitude of leakage currents into the side of the active region due to tunneling, which is expected to be lower in the case of an additional planarization regrowth.

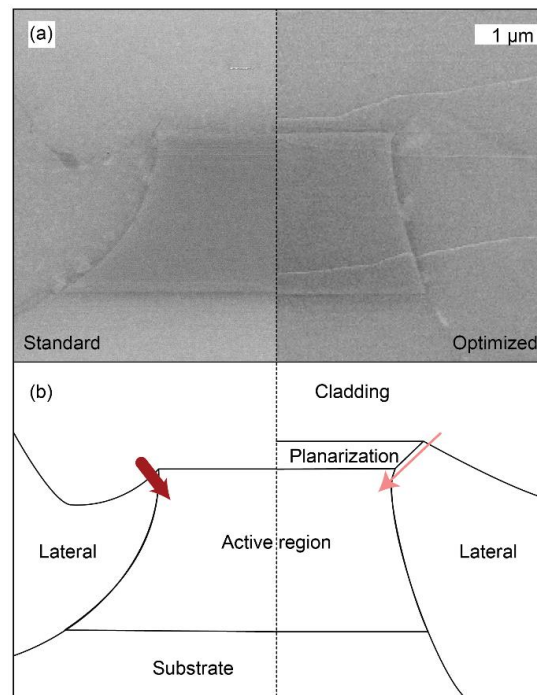


**Figure 4.** (a) Comparison of two SEM micrographs showing the laser facet of two devices, one fabricated with standard procedures, one with optimized procedures; and (b) schematic drawing highlighting the most important features depicted in (a). The red arrows indicate potential electrical leakage paths.

The lateral electrical isolation of the active region is crucial for the final device performance and is usually achieved by a Fe-doped ( $6 \times 10^{16} \text{ cm}^{-3}$ ) InP selective regrowth. The Fe dopants act as mid-gap traps for free carriers and, thus, pin the Fermi level in the forbidden bandgap at the interface between n-InP and Fe:InP, effectively blocking electronic current through this interface [12]. One potential leakage path is bulk leakage due to an insufficiently high Fe-doping concentration in the isolation regrowth. Current leakages can be detrimental for high-performing devices, since they increase the current threshold and add additional power to be dissipated which, in turn, increase the internal temperature and further deteriorate the performance. In order to further increase the resistivity of the lateral regrowth we investigated the effects of additional barriers made from AlInAs. The higher conduction band offset of this alloy increases the barrier height at the interface with InP and, thus, reduces the tunneling rate of electrons. This strategy to increase the resistivity was implemented through the introduction of a pair of 20 nm thick AlInAs layers, separated by a 50 nm thick InP layer, grown at the beginning and at the end of the lateral regrowth. The four different material configurations investigated were (i) pure InP:Fe as a reference; (ii) InP:Fe with AlInAs barriers; (iii) InP:Fe with AlInAs:Fe barriers; and (iv) an intrinsic InP layer followed by InP:Fe with AlInAs:Fe barriers (Figure 5a). The aim of the latter configuration is to additionally reduce photon reabsorption close to the active region in short-wavelength QCLs. The thickness of the doped InP:Fe core was 1.8  $\mu\text{m}$  in structure (i–iii) and 950 nm in structure (iv), where the i-InP was 850 nm thick. These layers were processed into square mesas with an n-InP cladding ( $2 \times 10^{18} \text{ cm}^{-3}$ ), an InGaAs top termination layer ( $2 \times 10^{19} \text{ cm}^{-3}$ ), and metallic top and bottom electrode. I-V profiling was performed to assess the resistivity at different voltages (Figure 5b,c). The voltage region most interesting for QCLs is highlighted in Figure 3c. The best performance is achieved by layer (iv) with an additional i-InP layer, followed by layer (iii), which features (as layer (iv) as well) AlInAs:Fe barriers. Layer (ii) with undoped barriers has similar performance to the reference InP:Fe (layer (i)).

Although in these particular experiments layer (iv) showed the best performance, it should be mentioned that in practice QCLs fabricated with layer (iii) show better results. Unfortunately, the benefit of reduced optical losses through the introduced i-InP layer is handicapped by electrical leakage. Finally we want to point out, that these results are strongly dependent on a well-controlled growth process in terms of material and gas purity, growth selectivity, and crystal conformity. QCLs are particularly prone to negative influences on crystal quality, due to the increased number of interfaces and switching between material systems.

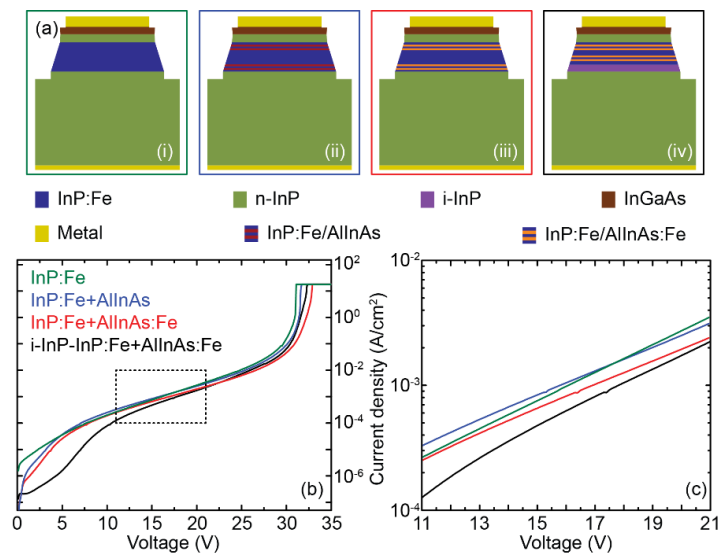


**Figure 5.** Summary of leakage optimization in the lateral regrowth. (a) Schematic drawings of the different test structures; (b) summary of I-V profile measurements from different test structures depicted in (a); and (c) a zoomed version of (b), focusing on the operation voltage region of mid-infrared QCLs, indicated in (b) by the dashed box.

For some specialized applications the regrowth of insulating Fe-doped InP can be performed using Hydride Vapor Phase Epitaxy (HVPE). Especially, structures where growth in high-aspect-ratio crevices (e.g., photonic crystals) is required, the regrowth technique should satisfy specific considerations. Firstly, the Fe concentration should be sufficiently large to impart semi-insulation to InP, *i.e.*, to pin the Fermi level near the mid bandgap of InP. This is particularly important in QCLs, since the electric fields in QCLs are in general very high (e.g., compared to interband lasers). The urgency of good electrical insulation further increases when high-aspect ratio crevices are deeply etched through the active region by an ICP process. Additionally, the actual Fe concentration in layers regrown in high-aspect-ratio crevices can depend on the growth rate and the orientation, and be different compared to growths on planar substrates (due to the orientation dependent doping [35]). Secondly, the regrowth should be selective, yield very good planarization and insensitive to the orientation of the etched mesas, to profile variations of the etched mesas (or pillars) caused by variation in process control. Finally, the regrowth should not result in appearance of crystal growth artifacts (e.g., “rabbit ears”) near the mesa (or pillar) edges [36]. HVPE is a technique that can meet all these demands [37].

The final regrowth step before the back-end processing of the metallic electrodes is a Si-doped InP cladding, which assures the uniform injection of carriers into the active region and, at the same time, guides the lasing modes with minimized optical losses. Engineering of the doping profile in this regrowth can provide additional shielding from leakage currents, while preserving its optical qualities. If the previously-mentioned planarization regrowth is terminated with a highly-doped ( $1 \times 10^{17} \text{ cm}^{-3}$ ) layer (40 nm), the doping at the beginning of the cladding layer can be kept relatively low ( $1 \times 10^{16} \text{ cm}^{-3}$ ). In addition, minimizing the free carrier absorption, the effect of this doping profile is that material along the lateral regrowth will be depleted and carriers will be effectively

funneled through the highly-doped contact layer prevailing only on top of the active region, thus, further reducing leakage through the Fe-doped InP regrowth. Closer to the metallization layer for the electrode contact the doping can be increased ( $3 \times 10^{18} \text{ cm}^{-3}$ ) to reduce the Schottky barrier at the interface between the top electrode and the cladding regrowth.

## 5. Optimized DFB-QCL Performance

In this section we apply the consideration of the previous section on short wavelength QCLs to benchmark the optimized process against the standard one. QCLs at short wavelengths are particularly interesting for spectroscopic applications, since the fundamental roto-vibrational transitions of many hydrocarbons and low-molecular species are in the 3–5  $\mu\text{m}$  range [6]. At the same time, low dissipation devices with high power are desirable, because these attributes would enable field-deployable operation of the devices. However, the development of QCLs on InP in this region is challenging, because the band offset between well and barrier required to achieve radiative intersubband transitions at a high enough energy can only be achieved in antimonide-based material systems or in the strained InGaAs/AlInAs material system [38–41]. We have previously published results of lasing action in the 3  $\mu\text{m}$  range [42]. In that work the device performances were impaired due to an unbalanced active region with an average 1.2% excess of indium and poor regrowth quality, resulting in leakage, high-threshold current densities, and mediocre power per QC period. Implementing the fabrication improvements described in the previous section yielded devices with narrow active waveguides, compared to previous works (Figure 6a). The improved grating fabrication step allows these devices to operate single mode at about 3.37  $\mu\text{m}$  [6] with a side mode suppression ratio (SMSR) better than 25 dB (Figure 6b). In Figure 4c a device with standard active region and fabrication is compared to an optimized version. The device sizes were 2.6 mm  $\times$  7  $\mu\text{m}$  (standard) and 0.6 mm  $\times$  2  $\mu\text{m}$  (optimized). The optimized device shown in Figure 4c is operating at half of the threshold current density compared to the standard device and its threshold current is as low as 25 mA.

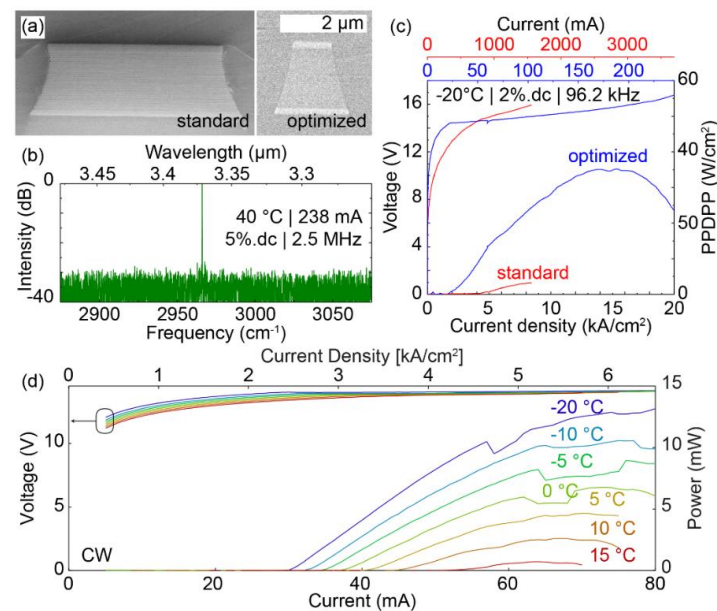


**Figure 6.** Summary of results for short-wavelength QCLs operating in the 3–3.5  $\mu\text{m}$  range. (a) SEM micrographs depicting facets of devices fabricated following the standard and optimized process protocol. Both images are at the same scale; (b) laser spectrum of a QCL emitting at 3.37  $\mu\text{m}$  with SMSR of 25 dB; and (c) light-current-voltage characteristics of devices fabricated following the standard and optimized process protocol. PPDPP stands for peak power density per period (*cf.* main text for a discussion of this parameter); and (d) continuous wave light-current-voltage characteristic of a QCL emitting around 3.3  $\mu\text{m}$  at different temperatures.

For the comparison of lasers from different growths, processes, and size we introduce the peak power density per period PPDPP parameter. The normalization area the PPDPP parameter refers to is the planar area of the active core. The facet area is taken into account through the normalization by the amount of active periods. The PPDPP of the optimized device reaches values of more than  $35 \text{ W/cm}^2$ , whereas the standard device reaches only approximately  $5 \text{ W/cm}^2$ . Although the PPDPP parameter neglects the precise shape of the active region, mirror losses, coupling related effects, and overlap factors, the comparison shown in Figure 6c is still convincing, because the optimized device giving rise to this data is shorter (associated with higher mirror losses) and narrower (associated by lower overlap factor) than the standard device. Additionally, a kink in the current-voltage curve (indicative for photo-induced current) and the large dynamic range ( $\sim 10:1$ ) of the optimized device is underlining the performance gains achieved by the improvements made in the active region design and processing steps. Furthermore, the application of a metallic and dielectric high-reflection coating on the back and the front facet, respectively, enables the devices from the optimized process to operate in CW up to  $15^\circ\text{C}$  and with output power in the range of 10 mW (Figure 6d). The current voltage characteristics show again characteristic kinks at the lasing threshold, a clear sign for photo-induced current. The data at currents below 4 mA is not shown because the high stability current driver used for this measurement (QCL2000, Wavelength Electronics, Inc., Bozeman, MT, USA) produces an open-circuit error for current below this threshold value.

## 6. QCL Arrays

For most spectroscopic applications (e.g., direct absorption measurements) reaching high power is of secondary concern and the primary interest is the ability to target absorption lines in different spectral locations simultaneously. A convenient but challenging way to achieve this goal is the monolithic integration of laser arrays on a single chip. An array of lasers arranged side by side can operate with completely isolated lasing cavities. However, it suffers from spatial separation of the light sources, and requires an external beam combination scheme [43–45]. Although such arrays can be operational, the spectroscopic requirements for low concentration gas sensing are very stringent and are best implemented with a single source coupled into an amplifier (e.g., a multi-pass interaction cell [46,47]).

Recently, we presented a surface emitting QCL array, which features regularly spaced single mode devices with a spectral coverage of  $175 \text{ cm}^{-1}$  [48]. The mode selecting cavity is based on distributed Bragg reflectors (DBR) with a second order extractor (Figure 7a). The distance between these two components was chosen in such a way to create a quarter wave shift defect mode in the center of the DBR stopband, allowing for a precise determination of the wavelength and, thus, a regular spectral spacing in the mode array. Additionally, we are introducing losses to the DBR sections, by only partly pumping them. This strategy helps to reduce the mode intensity at the facets, which effectively immunizes the mode selection process from the phase relation between the mode and the reflection at the facet. A chirp was introduced to the extractor grating in order to minimize the appearance of side lobes in the far-field. The radiation is emitted through a window in the top electrode. The resulting devices are arrays of 10 lasers, from which 9 out of 10 hit the desired mode (Figure 7b), with a SMSR better than 20 dB. Narrow far-field patterns (Figure 7c) confirm the functionality of the second order grating extractor with only few fringes originating from the metallic top contact.

The main advantages of such laser arrays are the amount of wavelengths per device area and the immunization of the mode from facet reflections. Nonetheless, the light sources are spatially separated, which will result in divergent beam paths when used in optical setups. Actual applications profit most from combined multi-wavelength beams, and thus such devices require an external beam combination scheme. Ideally, lasers emit a single beam with switchable wavelength, thus we monolithically integrated a beam combiner into the device. For this purpose we modified the previously mentioned laser array to emit the laser light through the substrate. These devices are identical to the ones presented in Figure 7a, besides the absence of the windows in the top electrode and the relocation of

the ground contact to the top surface of the chip (Figure 8a). For the purpose of relocating the ground electrode, an additional layer of conducting InP was grown on intrinsic InP before the MBE active region growth. This layer is exposed later in the fabrication process with the aim to position metallic ground electrodes (see Figure 8a) between the individual laser ridges [49].

In this approach the second order grating diffracts the radiation through the substrate. In order to collect this light we designed and bonded a second chip to the mirror-polished backside of the laser array via a varnish bond [49]. This chip featured a collector waveguide fabricated from a 3 μm thick InGaAs layer, which was equipped with second order gratings matching to those on the main laser ridge. This waveguide is thus collecting the radiation and guiding it to a single facet (schematically indicated with red arrows in Figure 8a). The device is therefore able to emit several laser wavelengths in the same beam, and render any external beam combination scheme obsolete. For a more detailed explanation of the devices presented in Figures 7 and 8 we refer the reader to the original published work [48,49].

Figure 8b shows a device with working light extraction and beam combination for seven out of nine designed lasers. Near-field measurements (Figure 8c,d) of the device while operating two different lasers prove that the collection waveguide works as intended and combines the emitted radiation into one single beam.

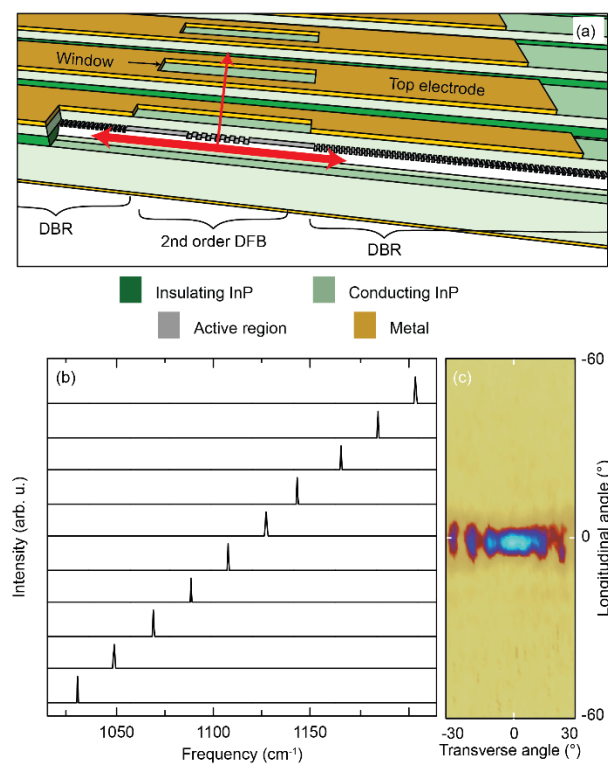


**Figure 7.** Surface emitting QCL array. (a) Schematic drawing of the surface emitting QCL array, revealing the first order DBRs, the second order DFB extractor, as well as the arrangement of the metallic top electrode including windows. The red arrows illustrate the path of the lasing mode; (b) laser spectra of the individual lasers in the array; and (c) far field intensity distribution of one laser in the array (transverse angle is rotated around the axis parallel to the active waveguide, longitudinal angle is rotated around the axis perpendicular to the active waveguide).

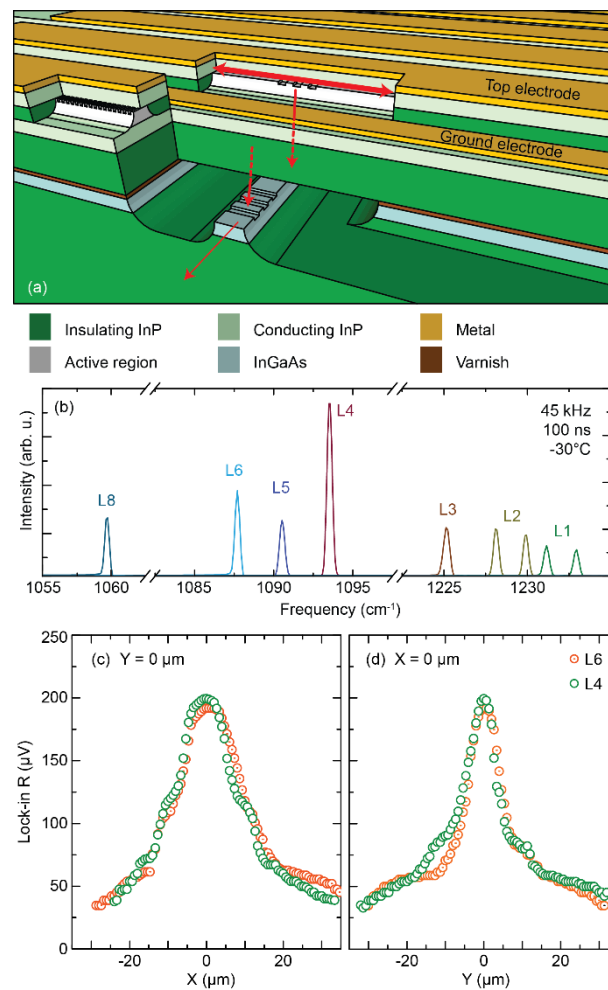


**Figure 8.** Substrate emitting QCL array with collection waveguide. (a) Schematic illustration of the QCL array, depicting the first order DBR, the second order DFB extractor and the bonded second order DFB collector waveguide. The red arrows illustrate the path of the lasing mode; (b) laser spectra of the individual lasers in the array; and (c,d) near-field amplitude scans of the collector waveguide facet along the X and Y axis during the separate operation of two lasers in the array.

### 7. Multi-Wavelength QCLs

Although the approach presented in the previous section is a way to combine the radiation of QCL arrays, it still suffers from a (non-fundamental) poor coupling efficiency and optimizing the final output power requires the precise adjustment of the gratings and the losses within the device. To apply QCL based trace-gas analysis of multiple species, a more robust device concept is needed. Ideally, the source can still emit several wavelengths in the same ridge but benefits from high output power and low power consumption. Such device concepts have been proposed previously for quantum-well and quantum-cascade lasers [50–52], however, they were incapable of single-wavelength emission and/or the two wavelengths were in close spectral proximity.

We developed QCLs that are able to emit two wavelengths individually within the same beam. These lasers are fabricated with the same process considerations as described in Sections 2–4. In contrast to the approach in Section 7 these devices do not require a wafer bonding step, because the lasers already emit from the same waveguide.

In the approach of multi-wavelength lasers, the amount of wavelengths per laser is limited because of detrimental effects such as internal etaloning, re-absorption, electrical crosstalk, and lasing on parasitic modes [53]. Therefore, expanding a spectroscopic setup to use more than two or three

wavelengths involves adding lasers to the system. The combination of these laser sources on a single beam path again requires an external beam combination scheme with optical elements (e.g., dichroic mirrors). However, the amount of devices can be reduced if each individual laser can simultaneously emit two to three wavelengths.

The devices consist of two sections, a front and a back section, with separate DFB gratings, corresponding to the desired wavelengths (Figure 9a). The active core is a hetero-stack of two different quantum cascades with a gain profile optimized to cover the desired spectral regions. In Figure 9b, a laser is shown that emits close to  $1600\text{ cm}^{-1}$  and  $1900\text{ cm}^{-1}$ , in order to target two different nitrous oxide species, which have relevance for environmental gas monitoring. The two sections are electrically isolated in order to allow individual pumping and to minimize cross-talk. These lasers show threshold current density of  $2.5\text{ kA/cm}^2$  and up to  $45\text{ mW}$  peak power in pulsed operation at room temperature, as demonstrated by light-current-voltage characteristics shown in Figure 9c. Such lasers can simply replace single wavelength devices in existing spectroscopic setups without the need for additional optical elements. In fact, the use of such a laser, together with suitable driving electronics has led to successful demonstrations of a spectroscopic application [53,54].

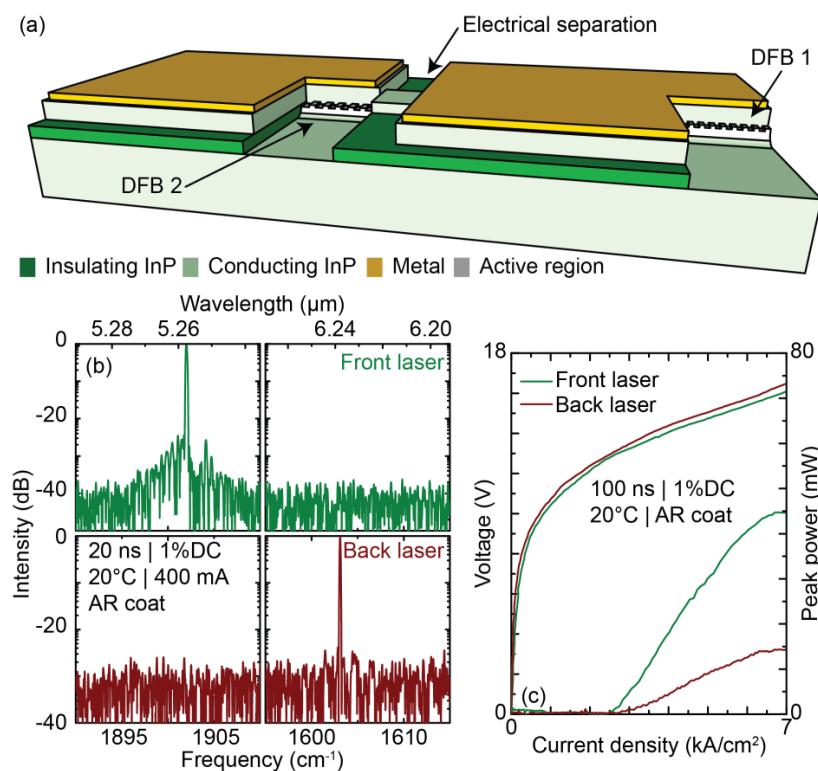


**Figure 9.** Dual-section DFB QCLs. (a) Schematic illustration of a dual-section DFB QCL revealing the two separate DFB gratings as well as the electrically separated top contact allowing for individual electronic control of the two laser wavelengths; (b) laser spectra of both section of a dual-section DFB QCL, operated individually; and (c) light-current-voltage characteristic of both sections of a dual-section DFB QCL individually operating at the wavelengths shown in (b).

## 8. Photonic Crystal QCLs

Some applications, such as open-path spectroscopy, benefit specifically from high-power single-mode operation with a proper beam shape [55,56]. Although DFB QCLs achieve high output power values, their maximum output power is limited due to the appearance of parasitic modes when increasing the length or width of the device. To achieve a high power output combined with high spectral purity, photonic crystal (PhC) lasers were proposed in the near-infrared [57].

The PhC approach as a mode control strategy was also applied in QCLs. The first attempts featured photonic crystals with air holes and plasmonic waveguiding, which provided a strong index contrast for mode selection, but the resulting poor heat extraction and high modal losses at the metal-semiconductor interface prevented room temperature operation [58]. Other approaches replaced one-dimensional DFB corrugations in the top cladding with a two-dimensional periodic structure, but despite the high optical power, the spectral purity was impaired by the low index contrast [59]. In this work we combine a buried heterostructure fabrication process [2,34,60] with a PhC deep-etched into the active region via inductively coupled plasma (ICP) etching, in order to combine the benefits of a strong material index contrast (~10%) and good heat extraction due to the monolithic contact between active region and regrown InP.

Finite difference time domain (FDTD) simulations of PhC (Figure 10) yield photonic band diagram (Figure 10b) and predict an effective refractive index contrast in this device geometry of about 7%, which is high enough to keep single mode operation over a large area (550  $\mu\text{m}$  side square). Primary laser action is designed to occur in the  $\Gamma^{(2)}$  point (marked green in Figure 10b) in order to keep a large enough period size for the fabrication process. The volume overlap factor of the mode in  $\Gamma^{(2)}$  with the active region is 0.44 enabling an efficient use of the gain.

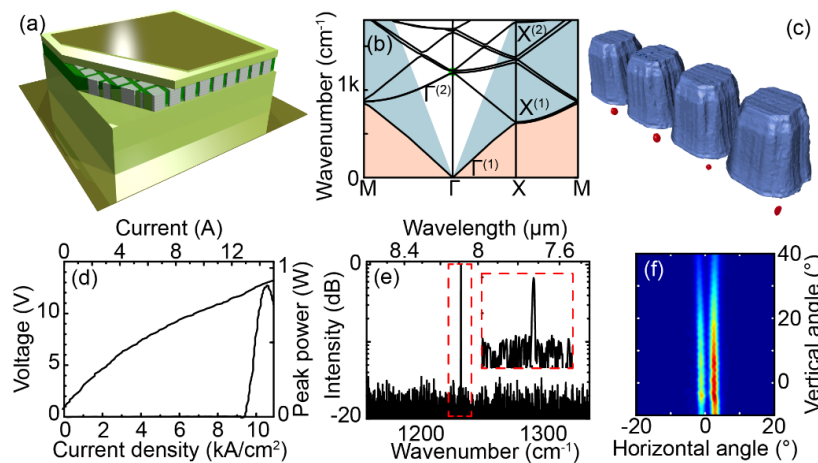


**Figure 10.** Buried photonic crystal QCLs. (a) Schematic illustration of the buried photonic crystal QCL. (b) Photonic crystal band structure, in which the most important symmetry points are indicated; (c) three-dimensional representation of a PhC structure, reconstructed from a focused ion beam SEM image stack; and (d) light current voltage characteristic of the photonic crystal QCL recorded at  $-20\text{ }^{\circ}\text{C}$ . (e) Laser spectrum of the photonic crystal QC; and (f) far field intensity pattern of the photonic crystal QCL.

For the fabrication of the buried-heterostructure PhC QCLs, we follow the same process protocol as for standard iBH lasers [34]. However, in contrast, the lateral regrowth of the Fe-doped semi-insulating InP grown around the pillars is performed with HVPE (due to considerations discussed in Section 3). The conductive InP cladding is grown with conventional MOVPE regrowth techniques.

To control the process we performed structural analysis through focused ion beam and scanning electron microscopy using slice and view strategy (Figure 10c and supplementary video), revealing the active region and the laterally regrown insulating InP. The small periodic voids appearing below the active region (Figure 10c, red) are due to an ICP over-etching during the definition of the active region pillars via inductive coupled plasma reactive ion etching. The over-etched surface at the bottom prevents proper regrowth conditions and creates voids filled with the atmospheric components in the HVPE reactor. Although the regrowth quality is sufficient in quality close to the active region, the process can still be tailored to avoid such artifacts altogether, in order to further improve the mode selection and the thermal performance.

Typical experimental results of such devices show a threshold of  $9.4 \text{ kA/cm}^2$  (Figure 10d) and a single mode behavior (Figure 10e). The threshold is twice as high as for separately processed Fabry-Perot reference devices from the same wafer, which is attributed to an incomplete Fe incorporation during the HPVE regrowth. The resulting lower barrier height in the isolating InP is responsible for leakage currents indicated in the shape of the IV characteristic. Despite all the process deficiencies, peak powers up to  $0.88 \text{ W}$  were recorded, which are approaching the best performing DFB devices [21]. In far field experiments two lobes are observed (Figure 10f). The recorded patterns are narrow in the horizontal direction, indicating that the lasing mode is a diffraction limited second order mode of the PhC mesa, and broad in the vertical direction conforming with diffraction through the height of the facet.

These results indicate that with further technological improvements (e.g., improvement of the PhC design, fully leveraging on the thermal dissipation through regrowth optimization) this approach can meet the requirements of photo acoustic spectroscopy, micro-surgery, or military countermeasures.

## 9. Conclusions

In this article we have summarized our latest achievements in the field of mid-infrared quantum cascade lasers. We have improved our active region growth by introducing material characterization protocols combining global and local techniques to assess crystallography, morphology, and chemistry. Advances in fabrication techniques, such as grating definition, waveguide etching, regrowth techniques, and optimization, as well as cladding engineering, have also helped to improve the device performances.

Our advances are demonstrated by well-functioning devices. We have demonstrated improved performances owing to a rigorous fabrication optimization in short-wavelength QCLs. The optimized devices are low dissipation emitters, single-mode, and operate in a continuous wave manner up to  $15 \text{ }^\circ\text{C}$ . Our advances in QCL process techniques also made the fabrication of a fully buried PhC QCL operating at room temperature possible. We further designed QCL arrays that, due to their grating concepts, are immune to the phase relation between mode and facet and are, therefore, suitable for a precise mode control. The issue of spatial separation is overcome by an additional fabrication step, where a collector waveguide equipped with second order DFB gratings is monolithically bonded to the backside of the laser array. Other multi-wavelength QCLs, which leverage on two electrically separated DFB gratings have been fabricated. These devices are facet emitters able to emit two wavelengths independently and are suitable light sources for simultaneous trace gas analysis of two or more gases. There is still room for improvements in terms of performance in all presented devices, and our repertoire of material characterization techniques is very suitable to identify the process steps requiring an optimization.

Nowadays, the QCL is a mature device and is at the verge to be included in full systems or products. The works we presented here, besides the performances themselves, consist of the building of a tool box for MIR QCL technology in general. All these efforts will allow better and cheaper integration in existing system as well as bring new possibilities for extending the use of QCL for novel and even unforeseen applications. For instance QCL frequency comb spectroscopy is a contemporary application of utmost interest since it can reach high performance in terms of spectral coverage in small-footprint systems [61–63]. All of the studies presented above will help to improve QCL frequency combs through an overall better fabrication, as well as to extend their use to other wavelength ranges or to allow spatial combination of combs.

**Supplementary Materials:** The following are available online at [www.mdpi.com/2304-6732/3/2/23/s1](http://www.mdpi.com/2304-6732/3/2/23/s1), Video S1: Slice and View focused ion beam sectioning of a buried photonic crystal QCL.

**Acknowledgments:** The authors acknowledge ScopeM and FIRST laboratories, ETH Zürich for the use of their facilities and continued assistance. In particular we thank Emilio Gini for MOVPE regrowth. Parts of this work have been funded by the Swiss National Foundation under the Nano-tera project “Irsens 2”, the European Union Seventh Framework Programme (FP7/2007-2013) under grant agreement N°317884, the collaborative Integrated

Project MIRIFISENS, the ETH Zurich Postdoctoral Fellowship Program, the Marie Curie Actions for People COFUND Program (N<sup>o</sup>FEL-27 14-2), as well as the Swiss National Foundation under the special measures project HIPROMIS. Furthermore funding was provided through the Swedish Research Council (VR) project number 2015-05470 and KTH Electrum Lab.

**Author Contributions:** M.J.S., R.P. and L.Y. drafted the manuscript. M.J.S., R.P., J.M.W., C.B., S.N., P.J. and B.H. designed, fabricated and analyzed devices. J.M.W. designed the active regions. W.M. and S.L. were responsible for HVPE regrowth. M.B. performed the M.B.E. growth of countless active regions. J.F. conceived and oversaw the experiments.

**Conflicts of Interest:** The authors declare no conflict of interest.

## Abbreviations

The following abbreviations are used in this manuscript:

APT	Atom probe tomography
AR	Anti-reflection
CW	Continuous wave
DBR	Distributed Bragg reflector
DFB	Distributed feedback
FDTD	Finite difference time domain
iBH	inverted buried heterostructure
ICP	inductively coupled plasma
IV	Current-voltage
LIV	Light-current-voltage
MBE	Molecular beam epitaxy
MOVPE	Metal-organic vapor phase epitaxy
PhC	Photonic crystal
PPDPP	Peak power density per period
QCL	Quantum cascade laser
SEM	Scanning electron microscope
SMSR	Side mode suppression ratio
TEM	Transmission electron microscope
XRD	X-ray diffraction

## References

1. Faist, J.; Capasso, F.; Sivco, D.L.; Sirtori, C.; Hutchinson, A.L.; Cho, A.Y. Quantum cascade lasers. *Science* **1994**, *264*, 553–556. [[CrossRef](#)] [[PubMed](#)]
2. Beck, M.; Hofstetter, D.; Aellen, T.; Faist, J.; Oesterle, U.; Ilegems, M.; Gini, E.; Melchior, H. Continuous wave operation of a mid-infrared semiconductor laser at room temperature. *Science* **2002**, *295*, 301–305. [[CrossRef](#)] [[PubMed](#)]
3. Bai, Y.; Bandyopadhyay, N.; Tsao, S.; Slivken, S.; Razeghi, M. Room temperature quantum cascade lasers with 27% wall plug efficiency. *Appl. Phys. Lett.* **2011**, *98*, 181102. [[CrossRef](#)]
4. Bismuto, A.; Blaser, S.; Terazzi, R.; Gresch, T.; Muller, A. High performance, low dissipation quantum cascade lasers across the mid-IR range. *Opt. Express* **2015**, *23*, 5477–5484. [[CrossRef](#)] [[PubMed](#)]
5. Hinkov, B.; Bismuto, A.; Bonetti, Y.; Beck, M.; Blaser, S.; Faist, J. Single mode quantum cascade lasers with power dissipation below 1 W. *Electron. Lett.* **2012**, *48*, 646–647. [[CrossRef](#)]
6. Wolf, J.M.; Riedi, S.; Süess, M.J.; Beck, M.; Faist, J. 3.36  $\mu\text{m}$  single-mode quantum cascade laser with a dissipation below 250 mW. *Opt. Express* **2016**, *24*, 662–671. [[CrossRef](#)] [[PubMed](#)]
7. Maulini, R.; Dunayevskiy, I.; Lyakh, A.; Tsekoun, A.; Patel, C.K.N.; Diehl, L.; Pflugl, C.; Capasso, F. Widely tunable high-power external cavity quantum cascade laser operating in continuous-wave at room temperature. *Electron. Lett.* **2009**, *45*, 107–108. [[CrossRef](#)]
8. Maulini, R.; Mohan, A.; Giovannini, M.; Faist, J.; Gini, E. External cavity quantum-cascade laser tunable from 8.2 to 10.4  $\mu\text{m}$  using a gain element with a heterogeneous cascade. *Appl. Phys. Lett.* **2006**, *88*, 201113. [[CrossRef](#)]

9. Wysocki, G.; Lewicki, R.; Curl, R.F.; Tittel, F.K.; Diehl, L.; Capasso, F.; Troccoli, M.; Hofler, G.; Bour, D.; Corzine, S.; *et al.* Widely tunable mode-hop free external cavity quantum cascade lasers for high resolution spectroscopy and chemical sensing. *Appl. Phys. B* **2008**, *92*, 305–311. [[CrossRef](#)]
10. Riedi, S.; Hugi, A.; Bismuto, A.; Beck, M.; Faist, J. Broadband external cavity tuning in the 3–4  $\mu\text{m}$  window. *Appl. Phys. Lett.* **2013**, *103*, 031108. [[CrossRef](#)]
11. Hugi, A.; Terazzi, R.; Bonetti, Y.; Wittmann, A.; Fischer, M.; Beck, M.; Faist, J.; Gini, E. External cavity quantum cascade laser tunable from 7.6 to 11.4  $\mu\text{m}$ . *Appl. Phys. Lett.* **2009**, *95*, 061103. [[CrossRef](#)]
12. Wittmann, A. *High-Performance Quantum Cascade Laser Sources for Spectroscopic Applications*; ETH: Zürich, Switzerland, 2009.
13. Hinkov, B.; Beck, M.; Gini, E.; Faist, J. Quantum cascade laser in a master oscillator power amplifier configuration with Watt-level optical output power. *Opt. Express* **2013**, *21*, 19180–19186. [[CrossRef](#)] [[PubMed](#)]
14. Lops, A.; Spagnolo, V.; Scamarcio, G. Thermal modeling of GaInAs/AlInAs quantum cascade lasers. *J. Appl. Phys.* **2006**, *100*, 043109. [[CrossRef](#)]
15. Vitiello, M.S.; Gresch, T.; Lops, A.; Spagnolo, V.; Scamarcio, G.; Hoyler, N.; Giovannini, M.; Faist, J. Influence of InAs, AlAs  $\delta$ -layers on the optical, electronic, and thermal characteristics of strain-compensated GaInAs/AlInAs quantum-cascade lasers. *Appl. Phys. Lett.* **2007**, *91*, 161111. [[CrossRef](#)]
16. Spagnolo, V.; Lops, A.; Scamarcio, G.; Vitiello, M.S.; di Franco, C. Improved thermal management of mid-IR quantum cascade lasers. *J. Appl. Phys.* **2008**, *103*, 043103. [[CrossRef](#)]
17. Pierściński, K.; Pierścińska, D.; Iwińska, M.; Kosiel, K.; Szerling, A.; Karbownik, P.; Bugajski, M. Investigation of thermal properties of mid-infrared AlGaAs/GaAs quantum cascade lasers. *J. Appl. Phys.* **2012**, *112*, 043112. [[CrossRef](#)]
18. Bismuto, A.; Terazzi, R.; Hinkov, B.; Beck, M.; Faist, J. Fully automatized quantum cascade laser design by genetic optimization. *Appl. Phys. Lett.* **2012**, *101*, 021103. [[CrossRef](#)]
19. Faist, J.; Beck, M.; Aellen, T.; Gini, E. Quantum-cascade lasers based on a bound-to-continuum transition. *Appl. Phys. Lett.* **2001**, *78*, 147–149. [[CrossRef](#)]
20. Bidaux, Y.; Terazzi, R.; Bismuto, A.; Gresch, T.; Blaser, S.; Muller, A.; Faist, J. Measurements and simulations of the optical gain and anti-reflection coating modal reflectivity in quantum cascade lasers with multiple active region stacks. *J. Appl. Phys.* **2015**, *118*, 093101. [[CrossRef](#)]
21. Lyakh, A.; Maulini, R.; Tsekoun, A.; Go, R.; Pflügl, C.; Diehl, L.; Wang, Q.J.; Capasso, F.; Patel, C.K.N. 3 W continuous-wave room temperature single-facet emission from quantum cascade lasers based on nonresonant extraction design approach. *Appl. Phys. Lett.* **2009**, *95*, 141113. [[CrossRef](#)]
22. Wittmann, A.; Gresch, T.; Gini, E.; Hvozdar, L.; Hoyler, N.; Giovannini, M.; Faist, J. High-Performance Bound-to-Continuum Quantum-Cascade Lasers for Broad-Gain Applications. *IEEE J. Quantum Electron.* **2008**, *44*, 36–40. [[CrossRef](#)]
23. Manninen, A.; Tuzson, B.; Looser, H.; Bonetti, Y.; Emmenegger, L. Versatile multipass cell for laser spectroscopic trace gas analysis. *Appl. Phys. B* **2012**, *109*, 461–466. [[CrossRef](#)]
24. Kosterev, A.; Wysocki, G.; Bakhirkin, Y.; So, S.; Lewicki, R.; Fraser, M.; Tittel, F.; Curl, R.F. Application of quantum cascade lasers to trace gas analysis. *Appl. Phys. B* **2007**, *90*, 165–176. [[CrossRef](#)]
25. Ren, W.; Jiang, W.; Tittel, F.K. Single-QCL-based absorption sensor for simultaneous trace-gas detection of  $\text{CH}_4$  and  $\text{N}_2\text{O}$ . *Appl. Phys. B* **2014**, *117*, 245–251. [[CrossRef](#)]
26. Titterton, D.H. Development of Infrared Countermeasure Technology and Systems. In *Mid-infrared Semiconductor Optoelectronics*; Krier, A., Ed.; Springer: London, UK, 2006; pp. 635–671.
27. Wagner, J.; Schulz, N.; Rösener, B.; Rattunde, M.; Yang, Q.; Fuchs, F.; Manz, C.; Bronner, W.; Mann, C.; Köhler, K.; *et al.* Infrared semiconductor lasers for DIRCM applications. In Proceedings of the Technologies for Optical Countermeasures, Wales, UK, 15–16 September 2008.
28. Kumar, C.; Patel, N. In Quantum cascade lasers and applications in defense and security. In Proceedings of the Photonics Society Summer Topical Meeting Series, Montreal, QC, Canada, 18–20 July 2011; pp. 49–50.
29. Huang, Y.; Kang, J.U. Corneal tissue ablation using 6.1  $\mu\text{m}$  quantum cascade laser. In Proceedings of the Proceedings of the International Society for Optical Engineering, San Francisco, CA, USA, 21 January 2012.
30. Hashimura, K.; Ishii, K.; Akikusa, N.; Edamura, T.; Yoshida, H.; Awazu, K. Coagulation and ablation of biological soft tissue by quantum cascade laser with peak wavelength of 5.7  $\mu\text{m}$ . *J. Innov. Opt. Health Sci.* **2014**, *7*, 1450029. [[CrossRef](#)]

31. Martini, R.; Bethea, C.; Capasso, F.; Gmachl, C.; Paiella, R.; Whittaker, E.A.; Hwang, H.Y.; Sivco, D.L.; Baillargeon, J.N.; Cho, A.Y. Free-space optical transmission of multimedia satellite data streams using mid-infrared quantum cascade lasers. *Electron. Lett.* **2002**, *38*, 181–183. [[CrossRef](#)]
32. Blaser, S.; Hofstetter, D.; Beck, M.; Faist, J. Free-space optical data link using Peltier-cooled quantum cascade laser. *Electron. Lett.* **2001**, *37*, 778–780. [[CrossRef](#)]
33. Hinkov, B.; Hugi, A.; Beck, M.; Faist, J. Rf-modulation of mid-infrared distributed feedback quantum cascade lasers. *Opt. Express* **2016**, *24*, 3294–3312. [[CrossRef](#)] [[PubMed](#)]
34. Bismuto, A. *Mid-Infrared Quantum Cascade Lasers*; ETH: Zürich, Switzerland, 2011.
35. Hammar, M.; Rodriguez Messmer, E.; Luzuy, M.; Anand, S.; Lourdudoss, S.; Landgren, G. Topography dependent doping distribution in selectively regrown InP studied by scanning capacitance microscopy. *Appl. Phys. Lett.* **1998**, *72*, 815–817. [[CrossRef](#)]
36. Cheng, L.; Fan, J.; Janssen, D.; Guo, D.; Chen, X.; Towner, F.J.; Choa, F.-S. Analysis of InP Regrowth on Deep-Etched Mesas and Structural Characterization for Buried-Heterostructure Quantum Cascade Lasers. *J. Electron. Mater.* **2011**, *41*, 506–513. [[CrossRef](#)]
37. Lourdudoss, S.; Kjebon, O. Hydride vapor phase epitaxy revisited. *IEEE J. Sel. Top. Quantum Electron.* **1997**, *3*, 749–767. [[CrossRef](#)]
38. Devenson, J.; Cathabard, O.; Teissier, R.; Baranov, A.N. High temperature operation of  $\lambda \approx 3.3 \mu\text{m}$  quantum cascade lasers. *Appl. Phys. Lett.* **2007**, *91*, 141106. [[CrossRef](#)]
39. Devenson, J.; Cathabard, O.; Teissier, R.; Baranov, A.N. InAs/AlSb quantum cascade lasers emitting at 2.75–2.97  $\mu\text{m}$ . *Appl. Phys. Lett.* **2007**, *91*, 251102. [[CrossRef](#)]
40. Revin, D.G.; Commin, J.P.; Zhang, S.Y.; Krysa, A.B.; Kennedy, K.; Cockburn, J.W. InP-Based Midinfrared Quantum Cascade Lasers for Wavelengths Below 4  $\mu\text{m}$ . *IEEE J. Sel. Top. Quantum Electron.* **2011**, *17*, 1417–1425. [[CrossRef](#)]
41. Bandyopadhyay, N.; Bai, Y.; Slivken, S.; Razeghi, M. High power operation of  $\lambda \sim 5.2\text{--}11 \mu\text{m}$  strain balanced quantum cascade lasers based on the same material composition. *Appl. Phys. Lett.* **2014**, *105*, 071106. [[CrossRef](#)]
42. Wolf, J.M.; Bismuto, A.; Beck, M.; Faist, J. Distributed-feedback quantum cascade laser emitting at 3.2  $\mu\text{m}$ . *Opt. Express* **2014**, *22*, 2111–2118. [[CrossRef](#)] [[PubMed](#)]
43. Yao, Y.; Hoffman, A.J.; Gmachl, C.F. Mid-infrared quantum cascade lasers. *Nat. Photon.* **2012**, *6*, 432–439. [[CrossRef](#)]
44. Lee, B.G.; Zhang, H.A.; Pflugl, C.; Diehl, L.; Belkin, M.A.; Fischer, M.; Wittmann, A.; Faist, J.; Capasso, F. Broadband Distributed-Feedback Quantum Cascade Laser Array Operating From 8.0 to 9.8  $\mu\text{m}$ . *IEEE Photonics Technol. Lett.* **2009**, *21*, 914–916. [[CrossRef](#)]
45. Mujagić, E.; Schwarzer, C.; Yao, Y.; Chen, J.; Gmachl, C.; Strasser, G. Two-dimensional broadband distributed-feedback quantum cascade laser arrays. *Appl. Phys. Lett.* **2011**, *98*, 141101. [[CrossRef](#)]
46. Tuzson, B.; Mangold, M.; Looser, H.; Manninen, A.; Emmenegger, L. Compact multipass optical cell for laser spectroscopy. *Opt. Lett.* **2013**, *38*, 257–259. [[CrossRef](#)] [[PubMed](#)]
47. Jouy, P.; Mangold, M.; Tuzson, B.; Emmenegger, L.; Chang, Y.-C.; Hvozdar, L.; Herzig, H.P.; Wagli, P.; Homsy, A.; de Rooij, N.F.; *et al.* Mid-infrared spectroscopy for gases and liquids based on quantum cascade technologies. *Analyst* **2014**, *139*, 2039–2046. [[CrossRef](#)] [[PubMed](#)]
48. Jouy, P.; Bonzon, C.; Wolf, J.; Gini, E.; Beck, M.; Faist, J. Surface emitting multi-wavelength array of single frequency quantum cascade lasers. *Appl. Phys. Lett.* **2015**, *106*, 071104. [[CrossRef](#)]
49. Süess, M.J.; Jouy, P.; Bonzon, C.; Wolf, J.; Gini, E.; Beck, M.; Faist, J. Single-mode quantum cascade laser array emitting from a single facet. *Photonics Technol. Lett.* **2016**, *28*, 1197–1200. [[CrossRef](#)]
50. Samuel, S.; Stella, N.E.; Peter, M.S.; Andrey, B.K. Exploring the wavelength range of InP/AlGaInP QDs and application to dual-state lasing. *Semicond. Sci. Technol.* **2015**, *30*, 044002.
51. Pozzi, F.; Rue, R.M.D.L.; Sorel, M. Dual-Wavelength InAlGaAs–InP Laterally Coupled Distributed Feedback Laser. *IEEE Photonics Technol. Lett.* **2006**, *18*, 2563–2565. [[CrossRef](#)]
52. Straub, A.; Gmachl, C.; Sivco, D.L.; Sergent, A.M.; Capasso, F.; Cho, A.Y. Simultaneously at two wavelengths (5.0 and 7.5  $\mu\text{m}$ ) singlemode and tunable quantum cascade distributed feedback lasers. *Electron. Lett.* **2002**, *38*, 565–567. [[CrossRef](#)]
53. Süess, J.M.; Hundt, M.P.; Tuzson, B.; Riedi, S.; Wolf, M.J.; Peretti, R.; Beck, M.; Looser, H.; Emmenegger, L.; Faist, J. Dual-Section DFB-QCLs for Multi-Species Trace Gas Analysis. *Photonics* **2016**, *3*, 24. [[CrossRef](#)]

54. Jágerská, J.; Jouy, P.; Hugi, A.; Tuzson, B.; Looser, H.; Mangold, M.; Beck, M.; Emmenegger, L.; Faist, J. Dual-wavelength quantum cascade laser for trace gas spectroscopy. *Appl. Phys. Lett.* **2014**, *105*, 161109. [[CrossRef](#)]
55. Nikodem, M.; Wysocki, G. Chirped Laser Dispersion Spectroscopy for Remote Open-Path Trace-Gas Sensing. *Sensors* **2012**, *12*, 16466–16481. [[CrossRef](#)] [[PubMed](#)]
56. Taslakov, M.; Simeonov, V.; Froidevaux, M.; van den Bergh, H. Open-path ozone detection by quantum-cascade laser. *Appl. Phys. B* **2005**, *82*, 501–506. [[CrossRef](#)]
57. Noda, S.; Yokoyama, M.; Imada, M.; Chutinan, A.; Mochizuki, M. Polarization Mode Control of Two-Dimensional Photonic Crystal Laser by Unit Cell Structure Design. *Science* **2001**, *293*, 1123–1125. [[CrossRef](#)] [[PubMed](#)]
58. Colombelli, R.; Srinivasan, K.; Troccoli, M.; Painter, O.; Gmachl, C.F.; Tennant, D.M.; Sergent, A.M.; Sivco, D.L.; Cho, A.Y.; Capasso, F. Quantum Cascade Surface-Emitting Photonic Crystal Laser. *Science* **2003**, *302*, 1374–1377. [[CrossRef](#)] [[PubMed](#)]
59. Bai, Y.; Darvish, S.R.; Slivken, S.; Sung, P.; Nguyen, J.; Evans, A.; Zhang, W.; Razeghi, M. Electrically pumped photonic crystal distributed feedback quantum cascade lasers. *Appl. Phys. Lett.* **2007**, *91*, 141123. [[CrossRef](#)]
60. Peretti, R.; Liverini, V.; Wolf, J.M.; Bonzon, C.; Süess, M.J.; Lourdudoss, S.; Metaferia, W.; Beck, M.; Faist, J. Room Temperature Operation of a Buried Heterostructure Photonic Crystal Quantum Cascade Laser. Available online: <http://arxiv.org/abs/1502.03940> (accessed on 4 May 2016).
61. Hugi, A.; Villares, G.; Blaser, S.; Liu, H.C.; Faist, J. Mid-infrared frequency comb based on a quantum cascade laser. *Nature* **2012**, *492*, 229–233. [[CrossRef](#)] [[PubMed](#)]
62. Khurgin, J.B.; Dikmelik, Y.; Hugi, A.; Faist, J. Coherent frequency combs produced by self frequency modulation in quantum cascade lasers. *Appl. Phys. Lett.* **2014**, *104*, 081118. [[CrossRef](#)]
63. Villares, G.; Hugi, A.; Blaser, S.; Faist, J. Dual-comb spectroscopy based on quantum-cascade-laser frequency combs. *Nat. Commun.* **2014**, *5*. [[CrossRef](#)] [[PubMed](#)]



© 2016 by the authors; licensee MDPI, Basel, Switzerland. This article is an open access article distributed under the terms and conditions of the Creative Commons Attribution (CC-BY) license (<http://creativecommons.org/licenses/by/4.0/>).